Nanoscale Horizons

ROYAL SOCIETY OF CHEMISTRY

COMMUNICATION

View Article Online
View Journal | View Issue

Cite this: *Nanoscale Horiz.*, 2025, 10, 1741

Received 31st March 2025,
Accepted 27th May 2025

DOI: 10.1039/d5nh00186b

rsc.li/nanoscale-horizons

Microfluidic fiber-spinning chemistry for hydrophilic–hydrophobic Janus membranes towards efficient interfacial solar evaporation†

Yin Li, Kebing Chen, Liangliang Zhu, Qing Li* and Su Chen

Janus nanofiber membrane has emerged as a promising solar-driven interfacial evaporator for seawater desalination. However, salt ion accumulation and crystallization persist during long-term operation, which remains a key challenge. In this work, we report a hydrophilic–hydrophobic Janus nanofiber membrane evaporator, which is prepared *via* continuous microfluidic electrospinning. This method allows *in situ* chemical reaction of tannin (TA) and Fe^{3+} to be carried out in a "Y" chip during the spinning process, enabling rapid, facile, and flexible fabrication of the nanofiber membrane. TA is rich in hydroxyl groups, which endows the bottom layer with hydrophilicity and electronegativity, thereby enhancing the water transport and Donnan effect. Thus, a high evaporation rate of 1.73 kg m^{-2} h^{-1} in pure water is achieved. More importantly, long-term stability in seawater desalination is realized with an evaporation rate of 1.68 kg m^{-2} h^{-1}, and there is no salt crystallization on the surface during continuous evaporation for 8 hours in 10 wt% NaCl solution. On the one hand, the bottom layer shows electronegativity, which is liable to immobilize cations Na^+ and repel anions Cl^-, achieving the purpose of salt resistance. On the other hand, the Janus structure also favors the redissolution of concentrated salts into raw water, further avoiding salt accumulation. This work offers a promising common strategy for constructing high-performance Janus evaporator, which will stimulate the development of seawater desalination.

New concepts

A microfluidic fiber-spinning chemistry technique was developed for facile fabrication of hydrophilic–hydrophobic Janus membranes towards efficient seawater evaporation. *In situ* chemical reaction of TA and Fe^{3+} is carried out in a "Y" chip during the spinning process, which enables rapid, facile and one-step synthesis of the PAN–TA–Fe^{3+} nanofiber membrane. By virtue of the Janus structure design and the Donnan effect, a seawater evaporation rate of 1.68 kg m^{-2} h^{-1} is obtained with long-term stability, making it a promising candidate for practical desalination applications.

Introduction

The rapid development of modern society brings ever-growing water pollution, exacerbating the scarcity of freshwater.[1,2] Advanced water purification technologies have been explored to mitigate water scarcity, such as reverse osmosis,[3] multi-effect distillation,[4] vapor compression distillation,[5] electrodialysis,[6] *etc.* However, these methods are energy-intensive and involve significant operational and financial costs.[7] Recently, solar desalination has emerged as a promising alternative due to its low cost, high energy efficiency, and environmental sustainability.[8] The main principle of this technique is converting solar energy into heat, which further promotes the generation of water vapor at the evaporation interface.[9,10] Significant advancements in energy efficiency and evaporation rates have been achieved by developing high-performance solar thermal materials (fabric,[11] sponge,[12] hydrogel,[13] wood,[14] *etc.*), optimizing evaporator designs, reducing evaporation enthalpy, and enhancing thermal energy management.[15–17]

Nanofiber membranes share distinct advantages of large surface area for heat transfer and porous structures for vapor release and water transport.[18,19] The uneven pore distribution minimizes heat loss and improves evaporation efficiency at the interface.[20] Therefore, nanofibrous membranes are particularly suitable for solar-driven interfacial evaporation. However, the accumulation of salts or contaminants at the heating interface in a single-layer evaporator is inevitable, which may hinder the delivery of water and steam and reduce the light absorption rate, thereby reducing the evaporation efficiency.[21] To solve this problem, hydrophilic/hydrophobic Janus membrane has emerged, featuring a hydrophobic top layer and a hydrophilic bottom layer.[22–24] The hydrophilic layer favors salt ion diffusion while the hydrophobic layer can block the salt, preventing salt accumulation on the top surface.[25–28] It has been proved that

State Key Laboratory of Materials-Oriented Chemical Engineering, College of Chemical Engineering and Jiangsu Key Laboratory of Fine Chemicals and Functional Polymer Materials, Nanjing Tech University, Nanjing 210009, P. R. China. E-mail: liqing1128@njtech.edu.cn

† Electronic supplementary information (ESI) available. See DOI: https://doi.org/10.1039/d5nh00186b

the Janus membrane effectively couples sunlight absorption with water transport, which is superior to the single-layer membrane, exhibiting high evaporation rate and low salt crystallization. For example, Liu *et al.*[29] reported a reconfigurable and self-healing Janus evaporator, showing enhanced interface adhesion and stable desalination rate of 1.34 kg m^{-2} h^{-1}. Li *et al.*[30] proposed a self-descaling Janus nanofibrous evaporator based on reversible solar-induced wettability transition, which exhibited a water evaporation rate of 1.76 kg m^{-2} h^{-1} and long-term stability. Bai *et al.*[31] designed a photo-hot water diode evaporator (P/S@P-CFs) based on sustainable natural collagen fibers. The hydrophilic and hydrophobic Janus wettability allows the P/S@P-CF to automatically supply water and desalinate seawater during operation, enabling significant local heating and efficient water evaporation (evaporation rate of 1.73 kg m^{-2} h^{-1}). Although significant progress has been made, yet the Janus membrane-based evaporator possesses the disadvantage of complex preparation processes, and salt ion accumulation and crystallization persist during long-term operation, weakening the solar energy absorption and blocking the vapor diffusion paths.[32] Therefore, it is desirable to explore a simple and common strategy for anti-scaling Janus membrane-based evaporators.

Recently, microfluidic spinning technology has been increasingly appreciated as a reliable strategy to construct interconnected porous nanofiber membranes, which allows precise control of fiber composition, structures, and functions.[33,34] In particular, by virtue of the microfluidic chip, it enables the occurrence of *in situ* fiber-spinning chemistry, that is, chemical reactions are carried out on spinning fibers.[35–37] It is envisioned that the microfluidic electrospinning method provides a powerful tool for preparation of Janus nanofiber membranes in a flexible and facile fashion. To solve the salt accumulation problem, the Donnan effect has been employed to counteract the formation of salt crystals through its single-charge properties.[38] In this case, either anions or cations are repelled by the repulsion effect of fixed charge, thus achieving salt resistance for sustained stability over the long term. For instance, the anionic solar evaporator is liable to immobilize cations Na^+, while the movement of anions Cl^- is hindered, which avoids salt accumulation.[39] Lv *et al.*[40] designed a polyanionic electrolyte ionization desalination strategy, realizing a stable evaporation rate of 1.68 kg m^{-2} h^{-1} in brine (15% salinity) and long-term operation for 3 days in seawater (9% salinity). It has also been proved that the anionic hydrogel could enhance the Donnan effect and restrict the diffusion of Cl^- to the evaporator, achieving a remarkable water evaporation rate in 15 wt% NaCl solution, as well as showing effective salt resistance during prolonged evaporation processes.[41] Despite progress having been made, the complexity of the preparation process remains a challenge.[42] Therefore, it is necessary to develop a simple, green, low-cost method for the preparation of Janus membranes to overcome the problem of salt deposition in desalination.

Herein, we designed a hydrophilic–hydrophobic Janus nanofiber membrane evaporator, where the hydrophilic layer is electronegative to enhance the Donnan effect, thus achieving a high evaporation rate and durability in seawater desalination. This work shares the following advantages. (1) For the Janus nanofiber membrane evaporator design, the top layer is composed of hydrophobic thermoplastic polyurethane (TPU) and carbon nanotube (CNT), and serves as the photothermal layer, while the bottom hydrophilic layer consists of polyacrylonitrile (PAN) and electronegative tannin (TA), contributing to more hydrogen bonds for rapid water transport, as well as boosting the Donnan effect to exclusive salt ions (Fig. 1a). (2) In terms of the preparation of the Janus nanofiber membrane, continuous microfluidic electrospinning method is employed. It should be noted that *in situ* chemical reaction of TA and Fe^{3+} is carried out in a "Y" chip during the spinning process, which enables rapid, facile and one-step synthesis of PAN–TA–Fe^{3+} nanofiber membrane (Fig. 1b). This method significantly simplifies preparation processes and improves production efficiency. (3) By virtue of the Janus design and the Donnan effect (Fig. 1c), the pure water evaporation rate of 1.73 kg m^{-2} h^{-1} is obtained under one-sun illumination, with an efficiency of 85.25%. Besides, it also demonstrates a high evaporation rate of 1.68 kg m^{-2} h^{-1} and long-term stability in seawater desalination, and there is no salt crystallization on the surface after continuous evaporation for 8 h in 10 wt% NaCl solution, making it a promising candidate for practical desalination applications. This study presents a common and simple approach for developing efficient Janus nanofiber membrane evaporators for long-term seawater desalination and wastewater treatment, which is conducive to the development of fiber membrane evaporators in the field of seawater desalination in the future.

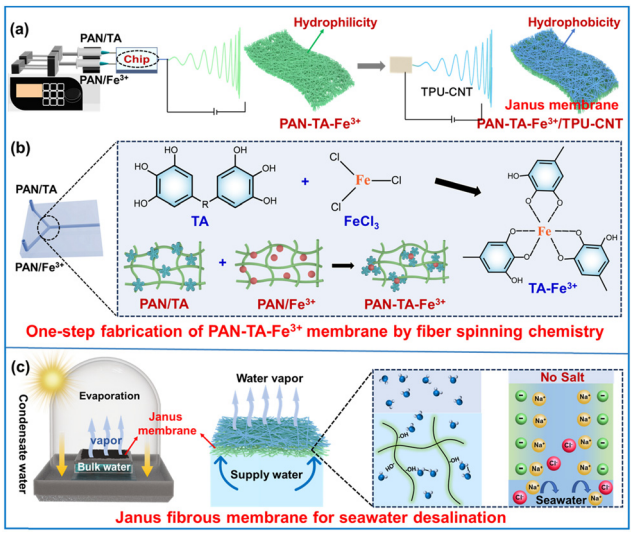

Fig. 1 (a) Schematic illustration of the fabrication of the PAN–TA–Fe^{3+}/TPU–CNT Janus fibrous membrane *via* continuous microfluidic electrospinning. (b) Schematic illustration of the *in situ* chemical reaction between TA and Fe^{3+} in microfluidic chip during spinning process. (c) Schematic illustration of the water evaporation process and mechanism.

Experimental

Materials

Polyacrylonitrile (PAN, M_w = 1 500 000) was purchased from Shanghai Macklin Biochemical Technology Co., Ltd. Thermoplastic

polyurethane (TPU, M_w = 1 300 000), *N*,*N*-dimethylformamide (DMF), tannic acid (TA), ferric trichloride ($FeCl_3$), multi-walled CNT (outside diameter of 10–20 nm, >95%), sodium chloride (NaCl), magnesium sulfate ($MgSO_4$), magnesium chloride ($MgCl_2$), calcium chloride ($CaCl_2$), potassium chloride (KCl), sodium bicarbonate ($NaHCO_3$), sodium bromide (NaBr), sodium hydroxide (NaOH), methylene blue (MB), methyl orange (MO), and rhodamine B (Rh B) were purchased from Shanghai Aladdin Biochemical Technology Co., Ltd. Deionized water was used in all the experiments.

Preparation of the PAN–TA–Fe^{3+} fibrous membrane *via* fiber-spinning chemistry

A certain amount of TA was added to 8.7 g DMF. After complete dissolution, 1.3 g PAN powder was added, followed by magnetic stirring at 500 rpm for 8 h to obtain a 13 wt% of PAN–TA spinning solution as solution A. Then a certain amount of $FeCl_3$ (TA : $FeCl_3$ = 4 : 1 M/M) was added to 8.7 g DMF. After complete dissolution, 1.3 g PAN powder was added and magnetically stirred at a speed of 500 rpm for 8 h to obtain a 13 wt% of PAN–Fe^{3+} spinning solution, defined as solution B. Then solution A and solution B were sequentially loaded into two syringes, which were connected with a "Y" chip. Both solutions were fed at the same constant feed rate (0.3 mL h^{-1}) through a steel needle (24 G). Finally, the solutions were well mixed in the microchannel, and the reaction between TA and Fe^{3+} was completed during the spinning process. PAN–TA–Fe^{3+} fibrous membranes with different TA–Fe^{3+} concentrations were obtained by microfluidic electrospinning for 3 h (voltage: 17 kV; distance from the receiver: 15 cm).

Preparation of the PAN–TA–Fe^{3+}/TPU–CNT Janus fibrous membrane

A certain amount of CNT was added into 8.7 g of DMF, forming a uniform dispersion after ultrasonic treatment for 30 min. Then 1.3 g of TPU was added, and the TPU–CNT spinning solution was obtained after magnetic stirring at 500 rpm for 8 h. For preparing the PAN–TA–Fe^{3+}/TPU–CNT Janus fibrous membrane, the TPU–CNT solution was electrospun on the as-prepared PAN–TA–Fe^{3+} fibrous membrane for 4 h at different parameters (voltage, 17 kV; spinning distance, 15 cm; feeding rate, 0.5 mL h^{-1}; needle tip, 24 G; rotation speed, 500 rpm). The hydrophilic PAN–TA–Fe^{3+} layer has a thickness of 102 μm, while the hydrophobic TPU–CNT layer has a thickness of 64 μm.

Solar evaporation experiments

A quartz beaker was used to evaluate the water evaporation performance, where a polystyrene foam lid with a square hole (2 × 2 cm^2) was used to eliminate other influence factors (temperature, 25 °C; relative humidity, 50%). The bottom of the film was connected to water with dust-free paper. The PAN–TA–Fe^{3+}/TPU–CNT Janus fibrous membrane was placed on a piece of commercial PS foam. The experiment was carried out by using a xenon arc lamp (CEL-PF300L-3A) and the light intensity is 1000 W m^{-2}. The water/seawater mass change was measured through gravimetric analysis, which was recorded every 10 min. The temperature changes were recorded using a FLIR E8 every 10 min. Finally, the conversion efficiency (η) was calculated according to eqn (1) and (2).[43,44]

$$m = \frac{\Delta m}{At} \quad (1)$$

$$\eta = \frac{m' h^*_{LV}}{P_{in}} \quad (2)$$

where m (kg m^{-2} h^{-1}) is the water evaporation rate, Δm (kg) is the water mass change in 1 h, A (m^2) is the photothermal area of membranes, and t is the duration of evaporation. η (%) is the efficiency of water evaporation and m' is the steady-state evaporation rate subtracted by that under dark conditions. h^*_{LV} denotes the water evaporation enthalpy (kJ kg^{-1}). P_{in} is the light intensity of evaporation. The infrared images were taken using an FLIR E8 infrared camera. Note: each measurement was performed 3 times for data accuracy. The average value was selected.

Characterization

Scanning electron microscopy (SEM, S-4800, Hitachi) was used to observe the morphologies of PAN, TPU, PAN–TA–Fe^{3+}, TPU–CNT, and PAN–TA–Fe^{3+}/TPU–CNT fibrous membranes. Fourier transform infrared spectrometer (FT-IR, American Thermo Nicolet-6700) was used to analyze the FT-IR spectra of the fibrous membrane. DSA100 (KRÜSS, Germany) was used to measure the water contact angles (WCAs) of fibrous membranes. An ESCAIAB250 XPS system with A1/Ka light source was utilized to measure the X-ray photoelectron spectroscopy (XPS) spectra of the fibrous membrane. UV-visible spectrophotometer (Lambda 750 S UV Spectrometer) was used to measure the absorbance spectra of the fibrous membrane. Inductively coupled plasma mass spectrometry (ICP-MS, Agilent 7500ce) was used to analyze the concentration of ions.

Results and discussion

CNT is a widely available, cost-effective and hydrophobic carbon-based material, which exhibits excellent light absorption and high photothermal conversion efficiency across a broad spectrum.[45,46] Thus, CNT and hydrophobic TPU were used to construct a photothermal layer for efficient solar energy capture. Besides, PAN and TA were selected as the hydrophilic layer for rapid water transport. TA is a typical natural polyphenol, which is easy to coordinate with metal ions due to the presence of multiple phenolic groups.[47–49] Notably, TA is easily soluble in water, which greatly affects the evaporation performance of the membrane. To avoid this problem, PAN–TA–Fe^{3+} nanofiber membrane was fabricated in a one-step and facile fiber-spinning chemistry method, where the reaction between TA and Fe^{3+} occurs in a Y type chip. The TA–Fe^{3+} complex is encapsulated in the PAN fiber membrane, showing strong coordination bonds to prevent the leakage of TA. Finally, the hydrophilic/hydrophobic Janus nanofiber membrane evaporator was fabricated through sequential microfluidic electrospinning of PAN–TA–Fe^{3+} and TPU–CNT. From the SEM images, an obvious Janus structure and highly open microporous network

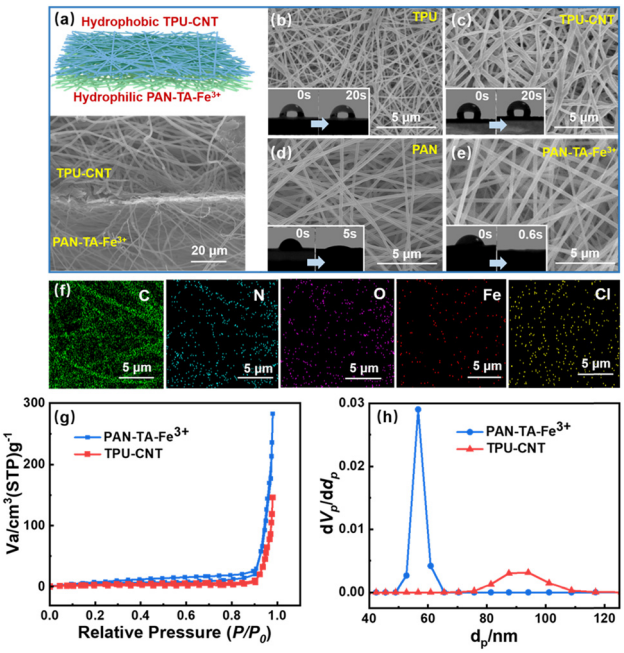

Fig. 2 (a) Schematic of the cross-section of the Janus fibrous membrane. SEM images and size distributions of (b) TPU, (c) TPU–CNT, (d) PAN and (e) PAN–TA–Fe^{3+} fibrous membrane. Inset: Water contact angle test of these fibrous membrane. (f) EDS mapping of C, O, N, Fe, Cl elements of PAN–TA–Fe^{3+}. (g) N_2 adsorption–desorption isotherms of PAN–TA–Fe^{3+} and TPU–CNT fibrous membrane. (h) Pore size distributions of PAN–TA–Fe^{3+}, TPU–CNT fibrous membrane.

are observed (Fig. 2a), which would support efficient water transport and vapor escape during solar-driven evaporation. As shown in Fig. 2b–e and Fig. S1 (ESI†), both pure TPU and PAN nanofiber exhibit smooth morphology with small diameters, 205 and 188 nm, respectively. With the loading of CNT and TA–Fe^{3+}, the nanofiber morphology becomes rough and thick, up to 427 and 373 nm, respectively. In terms of the PAN–TA–Fe^{3+} nanofiber membrane, the EDS mapping shows a uniform distribution of C, N, O, Fe, and Cl elements (Fig. 2f), confirming the uniform superiority of the fiber spinning chemistry method. Moreover, the TPU–CNT layer and PAN–TA–Fe^{3+} layer exhibit distinct wettability. The incorporation of CNT increases the surface roughness and hydrophobicity of the TPU–CNT fiber membrane, resulting in a contact angle of 116°, which remains unchanged after 20 s (Fig. 2c), whereas the contact angle of pure TPU is 96°. Conversely, the PAN–TA–Fe^{3+} layer exhibits super-hydrophilicity and the contact angle decreases to 0° within 0.6 s (Fig. 2e). In addition, we analyzed the pore structure and surface properties of each layer by using nitrogen adsorption–desorption measurements. It is found that PAN–TA–Fe^{3+} and TPU–CNT exhibit type II N_2 adsorption–desorption isotherms, confirming the presence of macropores (Fig. 2g and h). The pore size distribution of PAN–TA–Fe^{3+} and TPU–CNT reveals that they have an average pore size of 56.62 and 87.49 nm, respectively. According to Table S1 (ESI†), PAN–TA–Fe^{3+} exhibits a specific surface area of 22.91 $m^2\ g^{-1}$, which is greatly larger than that of TPU–CNT (2.41 $m^2\ g^{-1}$). Smaller fiber diameters result in reduced pore sizes, increased specific surface area, and enhanced water contact site, which is beneficial for steam escape to boost evaporation performance.[50] These results illustrate that the Janus nanofiber membrane displays asymmetric wettability, pore size distribution and specific surface area. The former could prevent salt accumulation during seawater evaporation, while the latter favors water transport and steam escape, which would synergistically boost evaporation.

To explore the chemical structure of the Janus fiber membrane, FTIR analysis was conducted. Fig. 3a illustrates the infrared spectrum of the original PAN membrane, showing characteristic peaks at 2937 cm^{-1} (CH_2 single bond) and 2242 cm^{-1} (C≡N group).[51] After loading TA, these peaks are significantly diminished, with new peaks emerging. Peaks between 3300 and 3400 cm^{-1} correspond to OH stretching vibrations from phenolic hydroxyl groups in TA, while peaks at 1564 cm^{-1} and 757 cm^{-1} indicate C–C stretching in aromatic rings and C–H out-of-plane bending in phenyl groups, respectively.[52] These findings confirm the encapsulation of TA in the PAN polymer network. In the spectrum of TPU, three characteristic peaks were observed around 3329, 2950, and 1072 cm^{-1}, corresponding to N–H tensile vibration, C–H bending vibration, and C–O–C tensile vibration, respectively. The peaks at 1731 cm^{-1} and 1527 cm^{-1} are attributed to the vibration of the –HN–COO– group.[53] Compared to pure TPU, the peak corresponding to the C=O group shows a slight shift (at 1703 cm^{-1}) when loading CNT (Fig. 3b), which is ascribed to the hydrogen bonding interactions between the TPU matrix and CNT.[54] XPS analysis was further performed to confirm the elemental composition and chemical structure of PAN/TPU and PAN–TA–Fe^{3+}/TPU–CNT membranes. Fig. 3c presents the XPS full spectrum, revealing three primary peaks for all membranes: C 1s

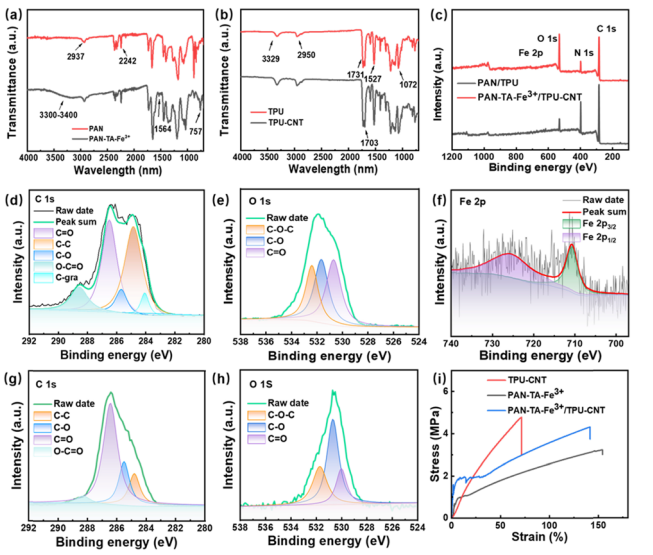

Fig. 3 (a) FT-IR spectra of PAN and PAN–TA–Fe^{3+} fibrous membrane. (b) FT-IR spectra of TPU and TPU–CNT fibrous membrane. (c) High-resolution XPS spectra of PAN/TPU and PAN–TA–Fe^{3+}/TPU–CNT fibrous membrane. XPS spectra of (d) C 1s, (e) O 1s and (f) Fe 2p of PAN–TA–Fe^{3+}/TPU–CNT fibrous membrane. XPS spectra of (g) C 1s and (h) O 1s of PAN/TPU fibrous membrane. (i) Stress–strain curves of PAN–TA–Fe^{3+}, TPU–CNT and PAN–TA–Fe^{3+}/TPU–CNT fibrous membrane.

(283.6 eV), N 1s (396.9 eV), and O 1s (529.5 eV). It is observed that the nitrogen peak intensity is weak, while the oxygen peak intensity is strong in the spectrum of the PAN–TA–Fe^{3+}/TPU–CNT membrane. From the C 1s spectrum in Fig. 3d and O 1s spectrum in Fig. 3e, both the O–C═O peak intensity and the C═O peak intensity are enhanced as compared with that of the PAN/TPU membrane (Fig. 3g and h), which is ascribed to the incorporation of TA.[48] Besides, a new CNT-related C-graphite peak at 284.1 eV was observed in the C 1s spectrum.[55,56] And new peaks at approximately 709.7 eV (Fe 2p) confirm the presence of Fe^{3+} in the Janus membrane (Fig. 3f).[57] The results provide strong evidence that the CNT and TA–Fe^{3+} are successfully loaded in the Janus membrane. Moreover, the mechanical properties of the membrane were evaluated, which plays an important role in its long-term use. The TPU–CNT layer exhibits higher tensile strength (4.76 MPa) than that of the PAN–TA–Fe^{3+} layer (3.21 MPa), while the PAN–TA–Fe^{3+} layer shows greater elongation at break (153.69%) compared to that of TPU–CNT (71.43%). Interestingly, the Janus membrane demonstrates relatively high tensile strength of 4.31 MPa and elongation at break of 141.46% (Fig. 3i), which could satisfy practical applications.

Light absorption and photothermal conversion are critical factors influencing the performance of Janus membrane evaporators.[58,59] The conjugated π-electron system of CNT efficiently absorbs light, which absorbs energy and transitions to higher energy states. When returned to the ground state, the energy is primarily released as heat, realizing the conversion of light energy into thermal energy.[46] Additionally, the porous structure of the Janus membranes would enhance light absorption while minimizing reflection. The combination of a porous structure, high porosity, and efficient absorption establishes a robust foundation for solar vapor generation. To obtain an optimal evaporation performance of the Janus fibrous membrane evaporator, the evaporation rate of the PAN–TA–Fe^{3+} layer was firstly evaluated. As shown in Fig. 4a, with TA–Fe^{3+} content increasing, the evaporation rate is gradually enhanced, peaking at 1.48 kg m^{-2} h^{-1} with 5 wt% TA–Fe^{3+}. When the TA–Fe^{3+} content is higher than 5 wt%, the uniformity of the fibrous membrane is compromised. Therefore, TA–Fe^{3+} content of 5 wt% is selected for the following evaporation experiments.

During evaporation, the photothermal conversion of the Janus membrane was monitored in real-time using an infrared camera and a thermometer. As the CNT content increases from 0 to 7 wt%, the surface temperature rises from 36.2 to 44.3 °C within 10 minutes correspondingly (Fig. 4b and c). The evaporation results are best illustrated in Fig. 4e, where the highest evaporation rate of 1.73 kg m^{-2} h^{-1} is achieved for the Janus evaporator, which is larger than that for single PAN–TA–Fe^{3+} and TPU–CNT fibrous membranes (Fig. 4a and Fig. S2, ESI†). Especially, when the CNT content is 0, 1, 3, 5, and 7 wt%, the evaporation rate is 0.76, 1.35, 1.53, 1.73 and 1.67 kg m^{-2} h^{-1}, while the photothermal conversion efficiency is calculated to be 30.9%, 65.14%, 77.08%, 85.25% and 81.43%, respectively (Fig. S3, ESI†). The micropores in the fiber membrane tend to be clogged at higher CNT contents, which hinders the upward evaporation channel of water vapor, resulting in a decrease in

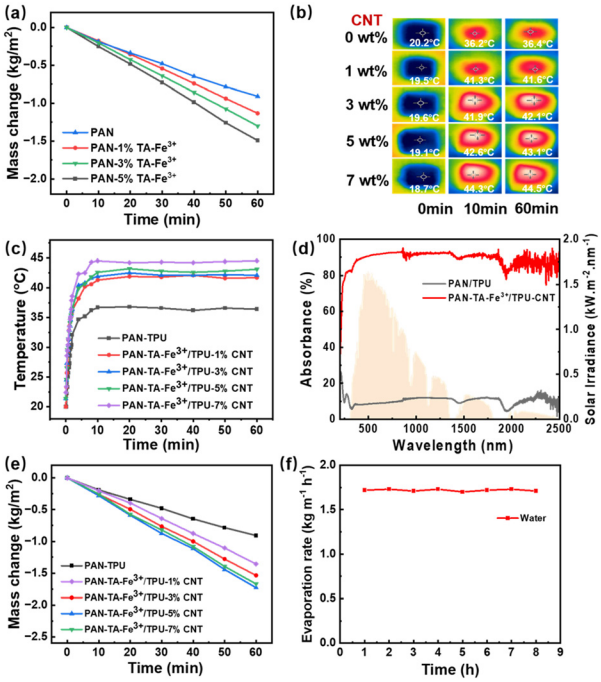

Fig. 4 (a) Water evaporation performance of single PAN–TA–Fe^{3+} fibrous membrane. (b) Infrared thermal images and (c) temperature of the top surface of PAN–TA–Fe^{3+}/TPU–CNT fibrous membrane *versus* time with different CNT contents. (d) Solar spectrum irradiance (AM 1.5 G) and the absorption spectrum of PAN/TPU and PAN–TA–Fe^{3+}/TPU–CNT fibrous membrane. (e) Water evaporation performance and (f) stability of PAN–TA–Fe^{3+}/TPU–CNT fibrous membrane.

water evaporation efficiency. Fig. 4d shows the solar spectrum irradiance (AM 1.5G) and the absorption spectrum of the PAN/TPU and PAN–TA–Fe^{3+}/TPU–CNT Janus fibrous membrane (CNT content of 5 wt%). It is found that the PAN–TA–Fe^{3+}/TPU–CNT fibrous membrane achieves broad and strong absorption across the ultraviolet to near-infrared spectrum, encompassing the full range of sunlight, which contributes efficient sunlight absorption to boost evaporation. Fig. 4f demonstrates the stability of the membrane over 8 evaporation cycles, which maintains a consistent evaporation rate of 1.7 kg m^{-2} h^{-1}, indicating excellent cycling stability and reusability.

The PAN–TA–Fe^{3+}/TPU–CNT Janus fibrous membrane has a bottom hydrophilic layer and an upper hydrophobic layer, with a porous structure and large porosity. In this case, the hydrophobic layer will not be wetted by the salt water, thereby isolating the precipitation of salt ions. To evaluate the solar evaporation efficiency of the Janus evaporator in brine, simulated seawater with varying NaCl concentrations (3.5–15 wt%) was used. Fig. 5a–c illustrate the water evaporation rates at different CNT contents under standard solar illumination. At 3.5 wt% NaCl concentration, the evaporation rates for CNT contents of 1%, 3%, 5%, and 7% were 1.35, 1.53, 1.68, and 1.57 kg m^{-2} h^{-1}, respectively. It should be noted that the evaporation rate shows no obvious decline with increasing NaCl concentration, revealing the outstanding evaporation performance in brine. Besides, there is no salt accumulation on the surface of the Janus membrane after continuous

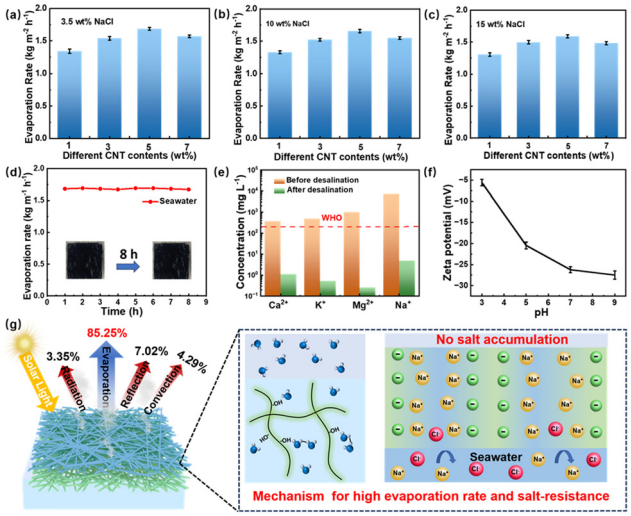

Fig. 5 (a)–(c) Evaporation rate of PAN–TA–Fe^{3+}/TPU–CNT fibrous membrane with different CNT contents for different NaCl concentrations. (d) Seawater evaporation performance of PAN–TA–Fe^{3+}/TPU–CNT fibrous membrane. Inset: Optical photographs of PAN–TA–Fe^{3+}/TPU–CNT fibrous membrane with seawater crystals before and after 8 h. (e) Ca^{2+}, K^+, Mg^{2+} and Na^+ concentration of the seawater before and after desalination. (f) Zeta potential of PAN–TA–Fe^{3+} under different pH values. (g) Schematic illustration of evaporation mechanism of the PAN–TA–Fe^{3+}/TPU–CNT Janus nanofiber membrane.

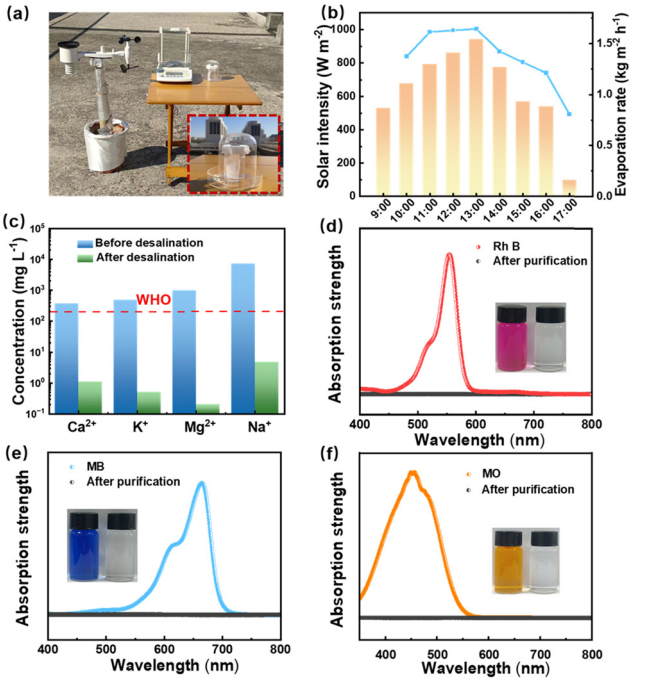

Fig. 6 (a) Digital photograph of an outdoor evaporation device. (b) Outdoor seawater evaporation performance of PAN–TA–Fe^{3+}/TPU–CNT Janus fiber membrane. (c) Ca^{2+}, K^+, Mg^{2+} and Na^+ concentration of the seawater before and after desalination. (d)–(f) UV-Vis spectroscopy before and after purification of Rh B, MB and MO solution.

evaporation for 8 h in 10 wt% NaCl solution, whereas obvious salt crystallization is observed on the single PAN–TA–Fe^{3+} membrane (Fig. S3, ESI†). We further employed laboratory-prepared simulated seawater to assess the evaporation stability, where each evaporation cycle was conducted under single sunlight exposure lasting one hour. As a consequence, the Janus evaporator maintains a stable evaporation rate of 1.68 kg m^{-2} h^{-1} for 8 hours (Fig. 5d) with no salt crystal accumulation on the membrane. The desalinated water, obtained by condensing vapor, was analyzed for ion concentrations (Na^+, K^+, Ca^{2+}, and Mg^{2+}) using ICP-MS. As depicted in Fig. 5e, the purified water exhibits significantly lower ion concentrations (Ca^{2+}, K^+, Mg^{2+}, and Na^+), well below WHO drinking water standards.[60]

TA is anionic under neutral or acidic conditions, and obtains a stronger negative charge by losing H^+ ions under alkaline conditions.[61,62] As shown in Fig. 5f, the electronegativity of the PAN–TA–Fe^{3+} membrane is enhanced with increasing pH value. When the pH value increases from 3 to 9, the zeta potential varies from −5.6 to −27.6 mV. This feature would enhance the Donnan effect to repel salt ions effectively in brine, achieving the purpose of salt resistance.[41] Fig. 6d depicts the schematic mechanism for the seawater evaporation of the Janus fibrous membrane. On one hand, the TPU–CNT layer exhibits excellent photothermal conversion capacity and hydrophobicity, which not only provides continuous heat but also prevents saltwater from wetting the surface, thereby avoiding salt deposition on the evaporation layer. On the other hand, the hydrophilic PAN–TA–Fe^{3+} layer contributes to continuous upward water transport, while the abundant phenolic hydroxyl groups enhance water/polymer hydrogen bonding (green, Fig. 5g) and weaken water/water hydrogen bonding, reducing vaporization energy and improving the evaporation rate.[23,63] Furthermore, TA–Fe^{3+} renders the membrane with electronegativity, enhancing the Donnan effect.[41] The negatively charged PAN–TA–Fe^{3+} layer adsorbs cations in salt ions *via* electrostatic interactions. During evaporation, co-ions are excluded, and counterions are also excluded by charge conservation, retaining specific salt ions and improving salt tolerance (Fig. 5g). Thus, the Janus structure traps concentrated brine below the hydrophobic/hydrophilic interface, preventing salt fouling on the TPU–CNT layer and maintaining consistent solar energy absorption and vapor release. Based on calculations of the overall energy balance (see the ESI,† eqn (S3)–(S5)),[64,65] the evaporator demonstrates an impressive evaporation efficiency of ∼85.25%, making it a promising candidate for practical desalination applications.

To assess the practical performance of the Janus evaporator, outdoor solar desalination was conducted on a sunny day in October in Nanjing, China, as shown in Fig. 6a. During the desalination process, data on the evaporation rate, solar intensity (Fig. 6b), and ambient temperature (Fig. S5, ESI†) were recorded. From 9:00 am to 6:00 pm, the evaporation rate initially increased, peaked at 1.68 kg m^{-2} h^{-1} at 1:00 pm, and then gradually declined, demonstrating excellent freshwater production capacity. The desalinated water was also analyzed for ion concentrations (Na^+, K^+, Ca^{2+}, and Mg^{2+}) using ICP-MS. As illustrated in Fig. 6c, the concentrations of Na^+, K^+, Mg^{2+}, and Ca^{2+} in the desalinated water were reduced by 3–4 orders of

magnitude, meeting WHO drinking water standards.[60] In addition, the Janus evaporator's purification capability was further evaluated using dye-contaminated wastewater. Due to the electronegative nature of the bottom layer of the Janus evaporator, the dye molecules can be effectively adsorbed by electrostatic action, while the evaporation rate keeps unchanged. The UV-Vis spectroscopy shows the concentrations (4 ppm) of organic dyes (MB, Rh B, and MO) before and after purification (Fig. 6d–f). Notably, the characteristic absorption peaks of the dyes disappear after purification, accompanied by a noticeable change in solution color, from dark to colorless. These results highlight the significant potential of the Janus evaporator for seawater desalination and wastewater treatment.

Conclusions

In summary, we propose the PAN–TA–Fe^{3+}/TPU–CNT Janus nanofiber membrane evaporator for high-performance seawater desalination. It is worth mentioning that the hydrophilic layer is fabricated using a facile and versatile fiber spinning chemistry method, which allows the *in situ* reaction of TA and Fe^{3+} during the spinning process, thereby realizing one-step fabrication of the PAN–TA–Fe^{3+} membrane. The Janus evaporator achieves a photothermal conversion efficiency of 85.25% and a water evaporation rate of 1.73 kg m^{-2} h^{-1}. More importantly, it also exhibits stability and salt resistance in brine, with an evaporation rate of 1.68 kg m^{-2} h^{-1} in seawater, and there is no salt crystal accumulation on the membrane for continuous evaporation of 8 hours in 10 wt% NaCl solution. Additionally, the maximum evaporation rate observed in outdoor experiments closely matches that achieved under simulated sunlight, highlighting its potential for practical seawater desalination. The outstanding evaporation performance could be ascribed to the following. On one hand, the TPU–CNT layer contributes to excellent photothermal conversion capacity and hydrophobicity, which prevents saltwater wetting and avoids salt deposition. On the other hand, the hydrophilic PAN–TA–Fe^{3+} layer favors continuous upward water transport, while its electronegativity enhances the Donnan effect to exclude salt ions. The synergistic effect enables continuous and stable seawater evaporation without salt accumulation, which will guide the design of seawater evaporators for practical applications. This work offers a simple fiber spinning chemistry method for constructing a high-performance Janus evaporator, realizing high evaporation rate and good salt tolerance. To meet practical application requirements, future works will be focused on improving long-term stability and recyclability of the Janus nanofiber membrane evaporator.

Author contributions

Yin Li: conceptualization, investigation, methodology, formal analysis, writing – original draft. Kebing Chen: formal analysis, validation. Liangliang Zhu: resources, supervision. Qing Li: resources, funding acquisition, writing – review & editing, supervision. Su Chen: conceptualization, funding acquisition, supervision.

Data availability

The authors declare that all data supporting the findings of this study are available within the article and its ESI.† Other supporting data are available from the corresponding author upon request.

Conflicts of interest

There are no conflicts to declare.

Acknowledgements

This work was supported by the National Natural Science Foundation of China (grant 22278225 to S. C. and grant 22378202 to Q. L.) and the Chinese Postdoctoral Science Foundation (grant 2022M721416 to Q. L.).

Notes and references

1 G. B. P. L. B. Chaffe, *Science*, 2023, **382**, 512–513.
2 T. Ma, S. Sun, G. Fu, J. W. Hall, Y. Ni, L. He, J. Yi, N. Zhao, Y. Du, T. Pei, W. Cheng, C. Song, C. Fang and C. Zhou, *Nat. Commun.*, 2020, **11**, 1–9.
3 L. F. Greenlee, D. F. Lawler, B. D. Freeman, B. Marrot and P. Moulin, *Water Res.*, 2009, **43**, 2317–2348.
4 H. Bamufleh, F. Abdelhady, H. M. Baaqeel and M. M. El-Halwagi, *Desalination*, 2017, **408**, 110–118.
5 B. Lin and M. Malmali, *Sep. Purif. Technol.*, 2023, **306**, 122568.
6 S. Al-Amshawee, M. Y. B. M. Yunus, A. A. M. Azoddein, D. G. Hassell, I. H. Dakhil and H. A. Hasan, *Chem. Eng. J.*, 2020, **380**, 122231.
7 F. E. Ahmed, R. Hashaikeh and N. Hilal, *Desalination*, 2020, **495**, 114659.
8 H. Liu, Z. Huang, K. Liu, X. Hu and J. Zhou, *Adv. Energy Mater.*, 2019, **9**, 1900310.
9 L. Zhang, Z. Xu, L. Zhao, B. Bhatia, Y. Zhong, S. Gong and E. N. Wang, *Energy Environ. Sci.*, 2021, **14**, 1771–1793.
10 P. Zhang, H. Wang, J. Wang, Z. Ji and L. Qu, *Adv. Mater.*, 2023, **36**, 2303976.
11 J. Hu, Y. Sun, Z. Liu, B. Zhu, L. Zhang, N. Xu, M. Zhu, J. Zhu and Z. Chen, *Prog. Mater. Sci.*, 2025, **150**, 101407.
12 B. Shao, Y. Wang, X. Wu, Y. Lu, X. Yang, G. Y. Chen, G. Owens and H. Xu, *J. Mater. Chem. A*, 2020, **8**, 11665–11673.
13 L. Li, C. Xue, Q. Chang, X. Ren, N. Li, J. Yang, S. Hu and H. Xu, *Adv. Mater.*, 2024, **36**, 2401171.
14 Z. Wang, Y. Yan, X. Shen, C. Jin, Q. Sun and H. Li, *J. Mater. Chem. A*, 2019, **7**, 20706–20712.
15 C. Chen, Y. Kuang and L. Hu, *Joule*, 2019, **3**, 683–718.
16 Z. Yu, R. Gu, Y. Tian, P. Xie, B. Jin and S. Cheng, *Adv. Funct. Mater.*, 2022, **32**, 2108586.
17 L. Geng, L. Li, H. Zhang, M. Zhong, P. Mu and J. Li, *J. Mater. Chem. A*, 2022, **10**, 15485–15496.
18 R. Tian, Y. Luo, Y. Teng, J. Zhang, Y. Liu, D. Li and L. Feng, *Sep. Purif. Technol.*, 2025, **359**, 130488.

19 P. Zhang, F. Liu, Q. Liao, H. Yao, H. Geng, H. Cheng, C. Li and L. Qu, *Angew. Chem., Int. Ed.*, 2018, **57**, 16343–16347.
20 J. Zhao, Z. Liu, S. C. Low, Z. Xu and S. H. Tan, *Adv. Fiber Mater.*, 2023, **5**, 1318–1348.
21 B. Nie, Y. Meng, S. Niu, L. Gong, Y. Chen, L. Guo, X. Li, Y.-C. Wu, H.-J. Li and W. Zhang, *Energy Environ. Sci.*, 2025, **18**, 3502–3525.
22 B. Xu, M. Ganesan, R. K. Devi, X. Ruan, W. Chen, C. C. Lin, H. T. Chang, E. Lizundia, A. K. An and S. K. Ravi, *Adv. Mater.*, 2025, **37**, e2406666.
23 H. Yao, P. Zhang, C. Yang, Q. Liao, X. Hao, Y. Huang, M. Zhang, X. Wang, T. Lin, H. Cheng, J. Yuan and L. Qu, *Energy Environ. Sci.*, 2021, **14**, 5330–5338.
24 Z. Sui, X. Xue, Q. Wang, M. Li, Y. Zou, W. Zhang and C. Lu, *Carbohydr. Polym.*, 2024, **331**, 121859.
25 J. Ju, Y. Huang, M. Liu, N. Xie, J. Shi, Y. Fan, Y. Zhao and W. Kang, *Sep. Purif. Technol.*, 2023, **305**, 122348.
26 J. Chen, J. L. Yin, B. Li, Z. Ye, D. Liu, D. Ding, F. Qian, N. V. Myung, Q. Zhang and Y. Yin, *ACS Nano*, 2020, **14**, 17419–17427.
27 L. Hou, N. Wang, L.-J. Yu, J. Liu, S. Zhang, Z. Cui, S. Li, H. Li, X. Liu, L. Jiang and Y. Zhao, *ACS Energy Lett.*, 2022, **8**, 553–564.
28 P. Huang, C. Huang, Y. Sun, Z. Zhao, L. Yang, H. Yang, L. Gong, W. Yang and H. Zeng, *Chem. Eng. J.*, 2024, **501**, 157824.
29 H. Liu, J. Gu, Y. Liu, L. Yang, L. Wang, J. Yu and X. Qin, *Nano Res.*, 2022, **16**, 489–495.
30 H.-N. Li, H.-C. Yang, C.-Y. Zhu, J. Wu, A. Greiner and Z.-K. Xu, *J. Mater. Chem. A*, 2022, **10**, 20856–20865.
31 Z. Bai, S. Huang, Y. Wu, X. Mei, J. Wang, Z. Zhang, L. Zhang, Y. Wei, G. He, A. Lu, M. Huang, X. Wang, X. Liu and J. Zhou, *Chem. Eng. J.*, 2025, **512**, 162703.
32 Y. Kuang, C. Chen, S. He, E. M. Hitz, Y. Wang, W. Gan, R. Mi and L. Hu, *Adv. Mater.*, 2019, **31**, 1900498.
33 H. Liu, L.-Y. Lu, Y. Zhang, J. Zhao, C. Liu, L. Zhu, Q. Li and S. Chen, *Nanoscale*, 2024, **16**, 12007–12012.
34 Q. Li, R. Chen, T. Cui, Y. Bai, J. Hu, J. Yu, G. Wang and S. Chen, *Adv. Healthcare Mater.*, 2024, **13**, 2304321.
35 Y. Song, X. Q. Yu and S. Chen, *J. Polym. Sci.*, 2023, **62**, 447–462.
36 R. Cheng, Z. B. Liang, L. Zhu, H. Li, Y. Zhang, C. F. Wang and S. Chen, *Angew. Chem., Int. Ed.*, 2022, **61**, e202204371.
37 X. Lu, Y. Hu, J. Guo, C. F. Wang and S. Chen, *Adv. Sci.*, 2019, **6**, 1901694.
38 W. Zhao, H. Gong, Y. Song, B. Li, N. Xu, X. Min, G. Liu, B. Zhu, L. Zhou, X. X. Zhang and J. Zhu, *Adv. Funct. Mater.*, 2021, **31**, 2100025.
39 X. Wang, L. Zhang, D. Zheng, X. Xu, B. Bai and M. Du, *Chem. Eng. J.*, 2023, **462**, 142265.
40 F. Lv, J. Miao, Z. Wang, J. Hu and D. Orejon, *Adv. Mater.*, 2025, **37**, e2410290.
41 X. Zhang, X. Zhang, L. Ma, B. Xu and H. Cong, *Sep. Purif. Technol.*, 2025, **353**, 128325.
42 Y. Cheng, Y. Luo, Y. Liu, D. Li and L. Feng, *New J. Chem.*, 2024, **48**, 12510–12515.
43 Z. Liu, B. Wu, B. Zhu, Z. Chen, M. Zhu and X. Liu, *Adv. Funct. Mater.*, 2019, **29**, 1905485.
44 C. Liu, Y. Peng and X. Zhao, *Carbohydr. Polym.*, 2021, **273**, 118536.
45 A. R. Biris, S. Ardelean, D. Lupu, I. Misan, C. Iancu, D. M. Bartos, I. R. Ilie, E. Dervishi, Y. Xu, A. Biswas and A. S. Biris, *Carbon*, 2011, **49**, 4403–4411.
46 X. Cui, Q. Ruan, X. Zhuo, X. Xia, J. Hu, R. Fu, Y. Li, J. Wang and H. Xu, *Chem. Rev.*, 2023, **123**, 6891–6952.
47 Z. Wang, J. Gao, J. Zhou, J. Gong, L. Shang, H. Ye, F. He, S. Peng, Z. Lin, Y. Li and F. Caruso, *Adv. Mater.*, 2022, **35**, 2209015.
48 Z. Wang, M. Han, F. He, S. Peng, S. B. Darling and Y. Li, *Nano Energy*, 2020, **74**, 104886.
49 C. Zhang, Z. Chen, Z. Xia, R. Z. Waldman, S.-L. Wu, H.-C. Yang and S. B. Darling, *Environ. Sci. Water Resour.*, 2020, **6**, 911–915.
50 B. Sun, M. Wu, X. Zhao, L. Wang, Y. Jia, Z. Yuan, H. Wu, J. Diao, G. He and X. Jiang, *Adv. Funct. Mater.*, 2024, **34**, 2406272.
51 X. Zhang, N. Yu, Q. Ren, S. Niu, L. Zhu, L. Hong, K. Cui, X. Wang, W. Jiang, M. Wen and Z. Chen, *Adv. Funct. Mater.*, 2024, **34**, 2315020.
52 Y. Xiao, D. Guo, T. Li, Q. Zhou, L. Shen, R. Li, Y. Xu and H. Lin, *Appl. Surf. Sci.*, 2020, **515**, 146063.
53 Y. Tian, M. Huang, Y. Wang, Y. Zheng, R. Yin, H. Liu, C. Liu and C. Shen, *Chem. Eng. J.*, 2024, **480**, 147899.
54 T. Guo, C. Li, J. Yang, P. Wang, J. Yue, X. Huang, J. Wang and X.-Z. Tang, *Composites, Part A*, 2020, **136**, 105974.
55 B. Alemán, M. Vila and J. J. Vilatela, *Phys. Status Solidi A*, 2018, **215**, 1800187.
56 T. I. T. Okpalugo, P. Papakonstantinou, H. Murphy, J. McLaughlin and N. M. D. Brown, *Carbon*, 2005, **43**, 153–161.
57 X. Zhang, Y. Yan, N. Li, P. Yang, Y. Yang, G. Duan, X. Wang, Y. Xu and Y. Li, *Sci. Bull.*, 2023, **68**, 203–213.
58 H. Jiang, X. Liu, D. Wang, Z. Qiao, D. Wang, F. Huang, H. Peng and C. Hu, *J. Energy Chem.*, 2023, **79**, 581–600.
59 Y. Wang, C. Wang, X. Song, S. K. Megarajan and H. Jiang, *J. Mater. Chem. A*, 2018, **6**, 963–971.
60 Safe Drinking-water from Desalination (World Health Organization, 2011), **https://apps.who.int/iris/bitstream/10665/70621/1/WHO_HSE_WSH_11.03_eng.pdf**.
61 L.-F. Ren, S. Zhang, Z. Ma, Y. Qiu, D. Ying, J. Jia, J. Shao and Y. He, *Desalination*, 2022, **541**, 116034.
62 Y. Deng, A. Zhang, Z. Zhang, Y. Xu, G. Li, M. Hankoy, M. Kitiwan, S. Wu, P. Dong, Y. Nan, W. Xu and J. Zhang, *J. Membr. Sci.*, 2024, **693**, 122333.
63 F. Z. Xingyi Zhou, Y. Guo, B. Rosenberger and G. Yu, *Sci. Adv.*, 2019, **5**, eaaw5484.
64 J. Su, Y. Xie, P. Zhang, R. Yang, B. Wang, H. Zhao, Y. Xu, X. Lin, J. Shi and C. Wang, *Desalination*, 2023, **566**, 116905.
65 J. Li, L. Mu, Q. Liu, Y. Zhang, R. Zhang, X. Zhu, C.-L. Sun, J. He and M. Qu, *Nano Energy*, 2024, **132**, 110394.

